



**HAL**  
open science

## Simultaneous measurements of dose and microdosimetric spectra in a clinical proton beam using a scCVD diamond membrane microdosimeter

Oluwasayo Loto, Izabella Zahradnik, Amelia Maia Leite, Ludovic de Marzi, Dominique Tromson, Michal Pomorski

### ► To cite this version:

Oluwasayo Loto, Izabella Zahradnik, Amelia Maia Leite, Ludovic de Marzi, Dominique Tromson, et al.. Simultaneous measurements of dose and microdosimetric spectra in a clinical proton beam using a scCVD diamond membrane microdosimeter. *Sensors*, 2021, 21 (4), pp.1314. 10.3390/s21041314 . cea-04551117

**HAL Id: cea-04551117**

**<https://cea.hal.science/cea-04551117v1>**


Submitted on 18 Apr 2024

**HAL** is a multi-disciplinary open access archive for the deposit and dissemination of scientific research documents, whether they are published or not. The documents may come from teaching and research institutions in France or abroad, or from public or private research centers.

L'archive ouverte pluridisciplinaire **HAL**, est destinée au dépôt et à la diffusion de documents scientifiques de niveau recherche, publiés ou non, émanant des établissements d'enseignement et de recherche français ou étrangers, des laboratoires publics ou privés.

Article

# Simultaneous Measurements of Dose and Microdosimetric Spectra in Clinical Proton Beam using scCVD Diamond Membrane Microdosimeter

Oluwasayo Loto <sup>1,†</sup> , Izabella A. Zahradnik <sup>1</sup> and A M. M. Leite <sup>2</sup>, Marzi Ludovic <sup>2</sup>, Dominique Tromson <sup>1</sup> and Michal Pomorski <sup>1,\*</sup>

<sup>1</sup> Université Paris-Saclay, CEA, List, F-91120 Palaiseau, France

<sup>2</sup> Institut Curie, PSL Research University, Radiation Oncology Department, Proton Therapy Centre, Centre Universitaire, 91898, Orsay, France

† Current address: Diamond Sensors Laboratory, Centre Digiteo, CEA LIST, 91191, Gif Sur Yvette, France

Version January 25, 2021 submitted to Sensors

**Abstract:** A single crystal chemical vapor deposition (scCVD) diamond membrane based microdosimetric system was used to perform simultaneous measurements of dose profile and microdosimetric spectra at Y1 proton passive scattering beamline of Center of Proton Therapy, Institut Curie in Orsay, France. To qualify the performance of the set-up in clinical conditions of hadrontherapy, the dose, dose rate and energy loss pulse-height spectra in diamond microdosimeter were recorded at multiple points along depth of a water-equivalent plastic phantom. The dose-mean lineal energy ( $\bar{y}_D$ ) values were computed from experimental data and compared to silicon on insulator (SOI) microdosimeter literature results. In addition, the measured dose profile, pulse height spectra, and  $\bar{y}_D$  values were benchmarked with numerical simulation using TOPAS and Geant4 toolkits. These first clinical tests of a novel system confirm that diamond is a promising candidate for tissue equivalent, radiation hard, high spatial resolution microdosimeter in beam quality assurance of proton therapy.

**Keywords:** Diamond, Proton therapy, Microdosimetry, Radiation detectors, Dosimeters, Sensors

## 1. Introduction

The use of proton beams for the treatment of cancers has gained considerable interest in recent years. This is observable from the increase in the number of proton beam centres around the world. For instance, in Europe there were 25 more proton beam centres constructed between 2009 and 2019 [1]. This is a result of the comparative advantage proton therapy offers over conventional photon radiation therapy. The absorbed energy of a proton beam increases with depth while that of photons decreases with depth giving clinical proton therapy a higher conformal dose delivery and hence less damage to critical tissues in patients than obtainable in photon radiation therapy. Like every other radiation procedures, there are some concerns around the undesirable effects of proton therapy, including necrosis of the healthy tissue in the proximity of treated tumor and cases of induced secondary cancers. The occurrence of secondary effects depends on the radiation dose, volume and the region irradiated [2]. Studies [3–5] have revealed the need for LET optimization to reduce any unwanted biological effects in proton therapy. The relative biological effectiveness (RBE) of radiation is defined as the ratio  $D_L/D_H$  where  $D_H$  is the absorbed dose of radiation, H at which the probability of a given biological effect is equal to that at an absorbed dose  $D_L$  of a reference radiation, L [6]. The RBE has been found to depend on the deposited physical dose, irradiated tissue and the quality of the beam which is measured by the linear energy transfer (LET). The RBE is an experimental quantity obtained from

31 irradiation studies on living cells. A proton RBE value of 1.1 is usually used for clinical therapy with  
32 photon radiation used as a reference [7]. Though the RBE model that proposes a value of 1.1 has been  
33 widely accepted, studies have shown that this value varies with proton energies (i.e along the depth  
34 dose profile), increasing significantly at the distal part of the Bragg Peak. Hence, an RBE weighted  
35 treatment plan could lead to the optimized dose delivery to patients with less important secondary  
36 effects occurrence, also in the case of proton therapy.

37 Microdosimetry has been used in the investigation of microdosimetric quantities of radiation field.  
38 The probability density  $d(y)$  together with the dose averaged lineal energy,  $\bar{y}_D$ , are physical quantities  
39 correlated with the biological effectiveness of the therapeutic beam obtainable from microdosimetry  
40 measurements. Tissue Equivalent Proportional Counters (TEPC) are well established for clinical  
41 microdosimetry. However, solid state microdosimeters have been introduced in clinical dosimetry as  
42 they offer higher spatial resolution, more robust and easy integration than conventional TEPCs.

43 Most solid state microdosimeters are based on silicon and have been introduced as an alternative  
44 to TEPCs. Due to the non-tissue equivalent nature of silicon, corrections must be made for effective  
45 extraction of dose parameters [9]. Over the years since the first publication on silicon microdosimeters,  
46 there have been continuous improvements in the design, structure and its efficiency [10–14]. Due to  
47 the limitations of silicon based microdosimeters, further development on the portability and efficiency  
48 of the TEPCs are also being considered. A compelling work is that of Conte [15] and Bianchi [16] on  
49 the use of sealed mini TEPC for proton beam therapy. Bianchi et al. observed similar microdosimetry  
50 spectra for mini TEPC and a  $\Delta E - E$  silicon microdosimeters at linear energies higher than  $8 \text{ keV} / \mu\text{m}$   
51 with discrepancies observed at lower LET values.

52 Rollet [17] first reported the use of artificial diamond for microdosimeters. Diamond ( $Z=6$ ) offers  
53 advantage due to its radiation hardness, near tissue equivalence ( $Z=7.5$ ) for photon radiation, resulting  
54 in less variable function for energy loss spectra conversion to water compared for example to silicon  
55 ( $Z=14$ ) [18]. In addition, some of the physical and electronic properties of diamond such as large-band  
56 gap, temperature stability, fast drift velocity and low capacitance, make diamond an interesting  
57 potential material for producing microdosimetric devices. Previous research works [20,21] have shown  
58 that single crystal diamond detectors exhibit good charge collection efficiency, homogeneity in the  
59 micro-sensitive volumes and can be used in measuring microdosimetric quantities in clinical beams.  
60 Using new device structures [22], improvements of the electric field geometry have also been proposed  
61 to maximise the charge collection efficiency and full potential of these detectors.

62 A diamond guard ring microdosimeter previously reported [24] by this group has shown the  
63 possibility of obtaining a sensor with full charge collection efficiency over broad range of linear energy  
64 transfer of ions at various energies. The proof of concept has prompted the authors to pursue the  
65 integration of this detector to simultaneously measure the depth dose profile and the microdosimetric  
66 spectra of a degraded 230 MeV clinical beam at the Proton therapy Center, Orsay, France.

## 67 2. Materials and Methods

### 68 2.1. scCVD diamond membrane Guard Ring (GR) prototype

69 The scCVD diamond membrane consists of four arrays of 16 sensitive volumes interconnected  
70 with bridges and bonded on a DIL20 chip carrier. Structurally, it comprises of an intrinsic diamond  
71 layer ( $12 \mu\text{m}$  thickness) sandwiched between two layers of metallic Aluminium electrodes. Further  
72 patterning of the top electrode and a chemical etching process was performed for the realization of  
73 multiple microsensitive volumes ( $\mu\text{SVs}$ ) surrounded by the guard ring structure as shown in figure  
74 1 (left). The critical dimensions have been chosen for the best signal to noise ratio in measurement  
75 conditions. Detailed description of the fabrication process of a guard-ring (GR) scCVD membrane  
76 microdosimeter and its charge transport characterization with an ion microbeam can be found in  
77 previous published work [24].

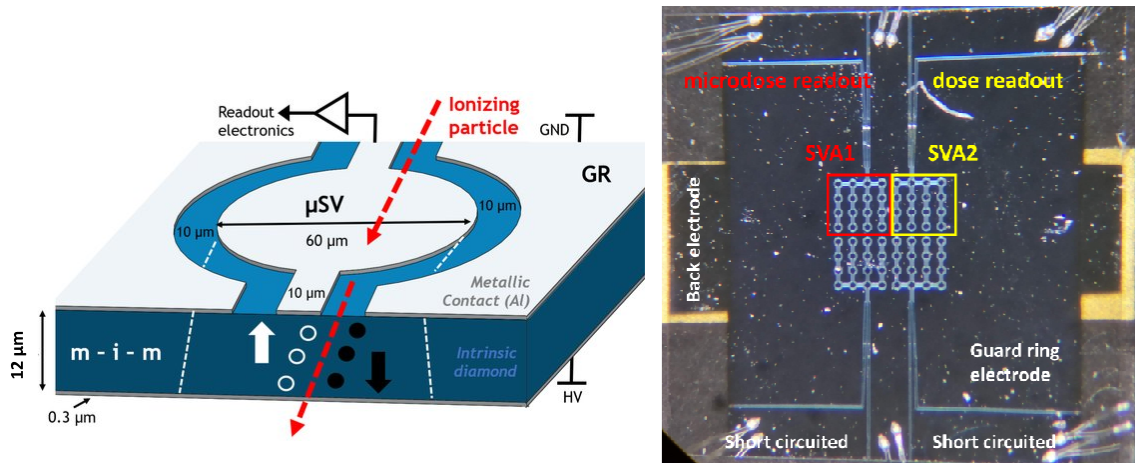


**Figure 1.** Left: the schematic representation of one micro-sensitive volume  $\mu SV$  of diamond GR microdosimeter prototype; Right: Optical micrograph of the diamond membrane with four sensitive microSVs arrays showing the  $\mu SV$ s marked with red (for microdosimetric read out) and yellow (dose read-out) color squares

78 As shown in figure 1 (right), the complete scCVD diamond membrane plate is arranged in four  
 79 arrays hereafter referred to as Sensitive Volume Arrays (SVA). Each array comprises of 16  $\mu SV$ s  
 80 interconnected with bridges and micro-bonded onto the chip carrier. In this device prototype, only two  
 81 (SVA1 and SVA2) of the four arrays of SVAs were used - one for microdosimetric spectra acquisition  
 82 and the other for dose measurements. The active area and lateral size of one SVA is 16  $\mu SV$ s is 0.045  
 83  $mm^2$  with each micro-sensitive volume having 60  $\mu m$  diameter. The total active area including bridges  
 84 is 0.057  $mm^2$ . The thickness of the diamond membrane is 12  $\mu m$  as confirmed from alpha particles  
 85 absorption spectroscopy and ion beam induced current technique with scanning transmission ion  
 86 microscopy approach [22].

## 87 2.2. Measurement set-up

88 A battery powered diamond based dosimetric and microdosimetric measurement system has  
 89 been developed. Although not fully integrated and miniaturized yet, here we present the first  
 90 proof-of-principle of operation of such a modular system in clinical conditions of a hadrontherapy  
 91 facility. Figure 2 (right) shows a diagram of the used set-up. The electrical signal induced by the proton  
 92 beam in both SVA of the diamond sensor (enclosed in an electrically screened plastic housing), is fed  
 93 to both a charge sensitive preamplifier Amptek CoolFET (CSA) for the purpose of microdosimetric  
 94 spectra measurements and a high precision Keithley 6517A pico-ammeter (pAM) for dose/dose rate  
 95 measurement. A fixed bias voltage of 15V (equivalent to electric field of 1.2  $V/\mu m$ ) is applied directly  
 96 to the back electrode of the diamond sensor from a voltage adjustment element (VADJ). The system is  
 97 powered by a 5V, 24 000 mAh PowerBank (PwBa).

98 Pre-amplified voltage pulses from CSA induced in the SVA1 of the diamond sensor by  
 99 single-particles are fed to a versatile, small size multi-channel analyzer (LabZY nanoMCA II [26]) with  
 100 integrated digital amplifier and WiFi module for data transfer. The MCA's digital amplifier shapes  
 101 and further amplifies the signal and processes the generated pulse-height spectra. Communication is  
 102 made with the personal computer (PC) through a wifi router. Physical connection between PC (placed  
 103 in control area) and the wifi router (placed in experimental area) is made by a 20 m long ethernet  
 104 cable. Beam induced DC current from the SVA2 of the sensor is fed to the picoammeter (placed in the  
 105 experimental) area through 2 m coaxial cable. Communication of the picoammeter with the PC, where  
 106 data is stored, is assured through a 20 m USB cable with three repeaters.

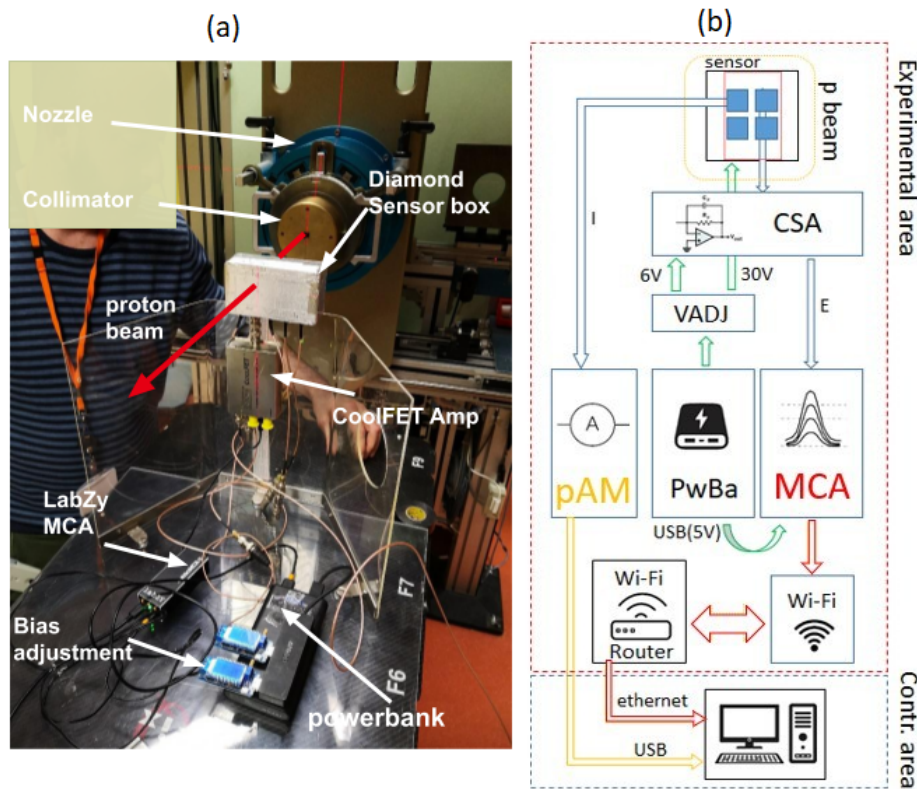


Figure 2. The Experimental set-up and the schematic of the experiment

### 107 2.3. Passive Scattering Beamline at the Proton Therapy Centre, Orsay

108 A proton beam of mean energy 230 MeV and energy spread 0.6 MeV ( $2\sigma$ ) generated by an IBA  
 109 C235 cyclotron, is degraded to 89 MeV in the isocenter by a range shifter. The range shifter contains  
 110 a combination of lexan and lead layers of different thicknesses. The beam is further scattered by  
 111 lead foils before entering the treatment room. A large brass collimator of  $4 \times 4 \text{ cm}^2$  was placed at the  
 112 end-point of the beam line, in order to obtain a homogenous 2D beam profile and at the same time  
 113 protect readout electronics from radiation damage. The water equivalent phantom SP34 made of white  
 114 polystyrene, type RW3 [27] in the form of various thicknesses 10 mm, 5 mm, and 1 mm square plates  
 115 were used to create dose profiles within target depth. These plates were gradually placed directly  
 116 before sensor housing during irradiation. The uncertainty of positioning depth was estimated to be  
 117 less than 0.1 mm, and it is mostly related to precision of plate fabrication and presence of air gaps  
 118 between the plates. All the components of the experiment including the geometry of the beam line  
 119 (shown in figure 3) and the diamond sensor were included in obtaining the energy loss spectra in  
 120 Geant4 and TOPAS numerical simulations. The Geant4 electromagnetic and hadronic physics models  
 121 were used in the simulation for describing particle trajectories. Details of these models can be obtained  
 122 in reference [28].

### 123 2.4. Energy calibration procedure for microdosimetric spectra measurements

124 Calibration was done in the laboratory prior to the measurements at a hadron therapy facility.  
 125 The procedure includes a combination of two techniques: First, the measurement of 5.486 MeV alpha  
 126 particles spectra from Am-241 with 300  $\mu\text{m}$  thick fully absorbing scCVD diamond detector in a vacuum  
 127 and secondly, a consecutive pulse generator calibration. A thick electronic grade scCVD detector was  
 128 placed in a vacuum chamber biased at 300 V ( $1\text{V}/\mu\text{m}$ ). Using an alpha particles radioactive source,  
 129 the pulse height spectra was recorded. A precise line spectra was obtained and fitted with a gaussian  
 130 distribution. The centroid at a fixed channel number corresponds to 5.486 MeV and at full width half



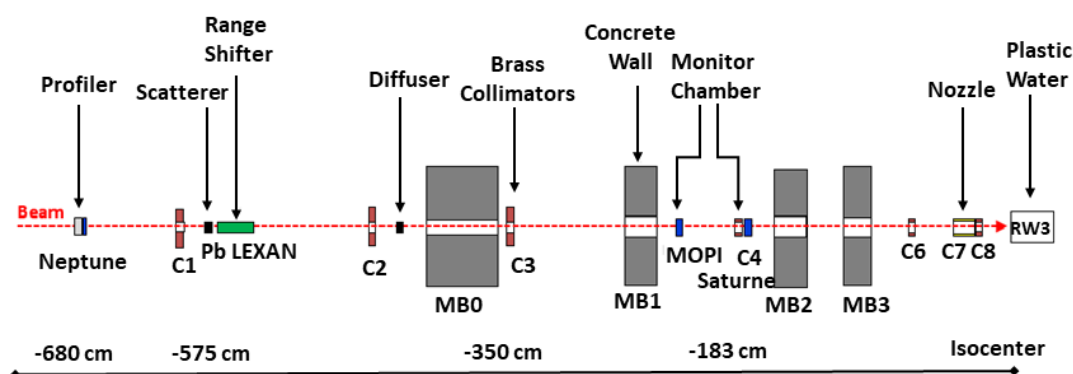


Figure 3. Y1 beam line geometry of IC-CPO used in TOPAS/Geant4 simulation

131 maximum of the alpha line of 0.3 %. Consequently an ORTEC pulse generator amplitude was adjusted  
 132 to match perfectly the measured alpha spectra line. Then, the thick scCVD detector was replaced by  
 133 the scCVD diamond membrane microdosimeter reported in this work. The system was re-calibrated with  
 134 the pulse generator, introducing 5 spectral lines at 5.486 MeV, 2.743 MeV, 1.37 MeV, 0.685 MeV, 0.343  
 135 MeV. No shift in the pulse generator peak at 5.486 MeV was observed compared to the measurement  
 136 system with thick diamond detector, indicating negligible influence of different detector capacitance  
 137 on the calibration process.

### 138 3. Results

#### 139 3.1. Dosimetric performance of the system

140 Figure 4 presents beam induced current curves measured under 30s irradiations at various depths  
 141 of plastic water phantom. The plateaus of the presented curves corresponds to relative dose rate of used  
 142 proton beam. A remarkably low leakage current (less than  $10^{-13}$  A) can be observed on the diamond  
 143 sensor for beam-off conditions. The beam induced charge was obtained by integrating the induced  
 144 current over the irradiation window (the induced charge corresponds to relative absorbed dose). The  
 145 maximum dose (induced charge) is obtained at 54 mm of plastic water depth marking the maximum  
 146 peak of the depth dose profile. Comparison between dose rate, instantaneous induced current at the  
 147 plateau level and dose integrated induced current curves (induced charge) within the irradiation time  
 148 window is presented in figure 5. It shows a perfect agreement between both quantities indicating  
 149 the possibility of fast scanning in water phantoms if only constant beam current is guaranteed at the  
 150 accelerator level.

151 To check reproducibility of the dose measurements, additional runs were performed for each  
 152 depth of the depth dose profile. Three irradiations were performed at each depth and at the same  
 153 irradiation times. Spread between measured values for each profile point was below 2%. This includes  
 154 uncertainty of precision of dose delivery by accelerator. The result also shows the good quality of the  
 155 underlying diamond material. Additionally, to our knowledge the presented sensor is the smallest  
 156 volume  $6.84 \times 10^{-4} \text{ mm}^2$  dosimeter available, which could be a perfect instrument for precise dose  
 157 measurements in small-field, microbeams and mini beam dosimetry.

#### 158 3.2. Energy loss spectra

159 The energy loss spectra obtained from labZY MCA of the calibrated diamond GR microdosimeter  
 160 is presented in figure 6. Only three measurements, related to the characteristics points of the depth  
 161 dose profile are shown. i.e (a) at the plateau (30 mm), (b) at the Bragg peak (BP) maximum (55 mm  
 162 depth) and (c) the distal end of the BP (69 mm). The corresponding Geant4 simulated energy spectra at

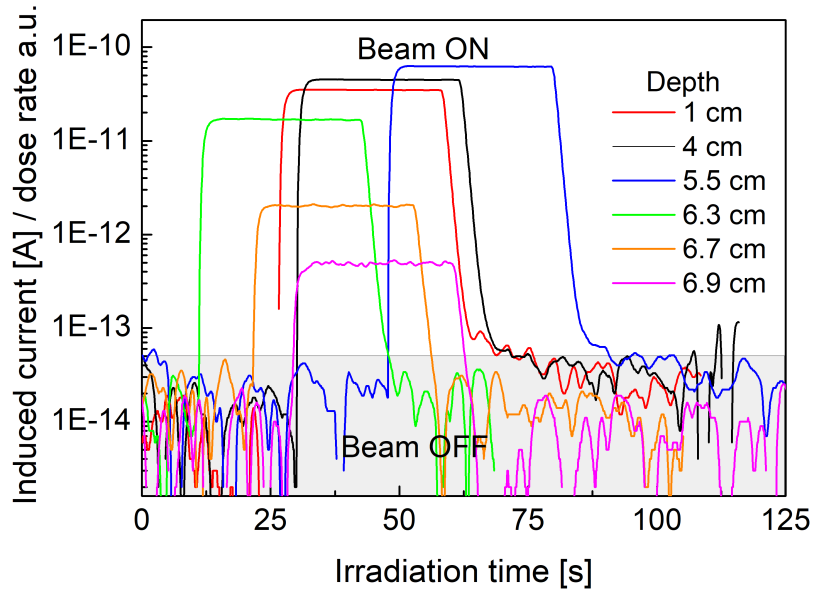


**Figure 4.** Proton Beam Induced Current in diamond GR microdosimeter at various depth of plastic water phantom

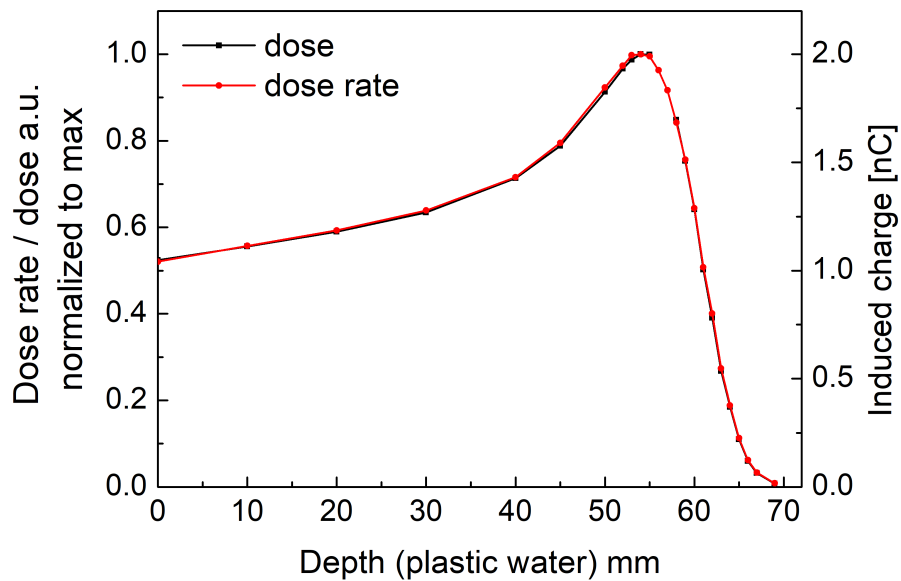


**Figure 5.** Comparison between measured induced current (dose rate profile) and measured induced charge (dose profile) for 230 MeV proton beam degraded to 89 MeV

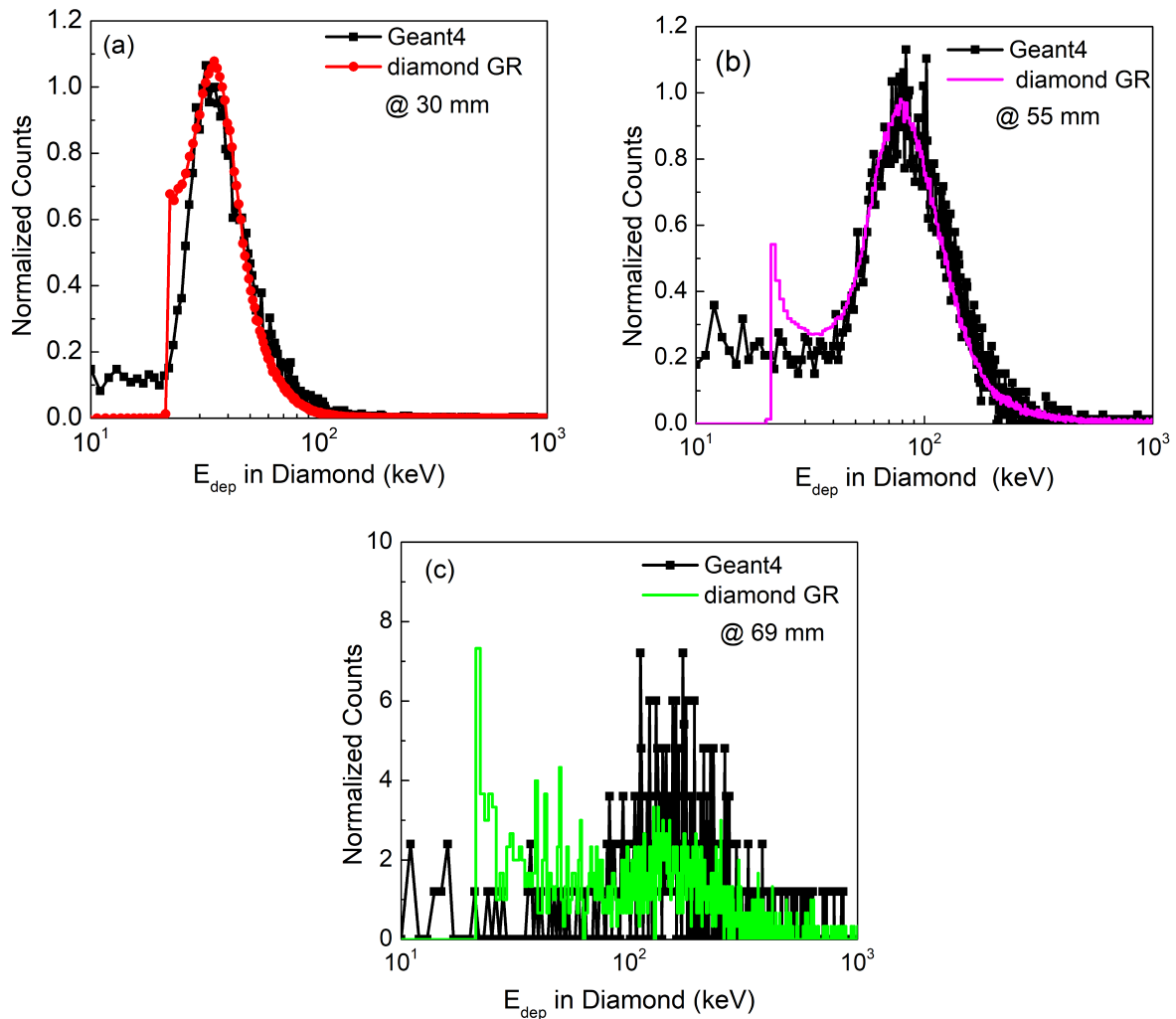


**Figure 6.** Selected measured calibrated pulse-height spectra obtained along depth dose profile at (a) 30 mm (b) 55 mm (c) 69 mm. Counts have been normalised to the primary proton peak.

163 each characteristic point is included in figure 6. There is a very good agreement between the measured  
 164 spectra and the simulation result in terms of distribution shape, peak position and its width.

165 In addition, a progressive shift of the peak position of the energy loss spectra towards higher  
 166 energies and broadening of the spectrum is observable with depth of water. This is due to protons  
 167 being slowed down towards the BP. Also, there is an expected reduction in the intensity with depth. A  
 168 low energy tail at around 22.25 keV is observed and become more pronounced at higher depth. This  
 169 low energy tail was previously associated with the incomplete charge collection efficiency (CCE) due  
 170 to the charge sharing between  $\mu\text{SV}$  and the guard ring electrode [24]. The measured spectra have a  
 171 cut-off at 20 keV that corresponds to the current limit of the measurement set-up due to the electronic  
 172 noise.

### 173 3.3. Water-equivalent microdosimetric spectra

174 By using a diamond-water conversion factor of 0.32 [25], the measured energy deposition spectra  
 175 obtained with the diamond GR microdosimeter was converted to water-equivalent microdosimetric  
 176 spectra  $yd(y)$ . In general, we observe that microdosimetric distributions shift towards higher energy  
 177 values with increasing depth in plastic water phantom. Due to the nature of the spectra transformation



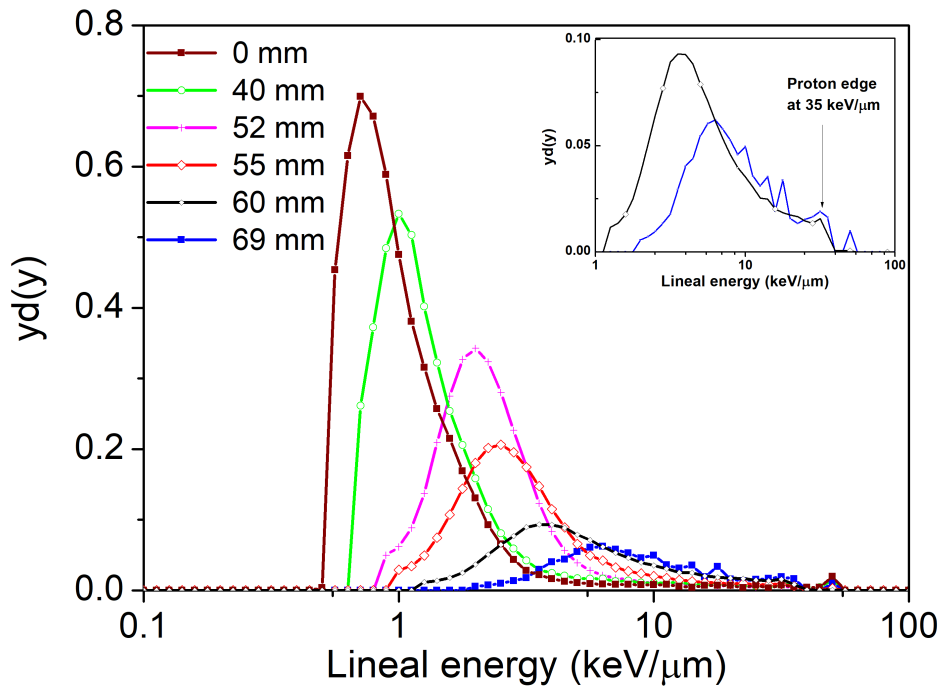


**Figure 7.** Experimental microdosimetric spectra obtained from GR diamond microdosimeter in plastic water phantom at depth of 0, 40, 52, 55, 60 and 69 mm. Inset: A zoom on the spectra at 60 and 69 mm. Proton edge at  $35 \text{ keV}/\mu\text{m}$  corresponds to protons of 1.3 MeV with stopping range of approximate  $12 \mu\text{m}$  in diamond equal to the sensor thickness.

178 process, the previously identified low energy tail in pulse-height spectra is still visible but does not  
 179 significantly contribute to the microdosimetric spectra area and thus to the calculated  $\bar{y}_D$  values. To  
 180 confirm this, we performed a cut-off for four measured pulse height distributions removing low energy  
 181 tails prior to the transformation to microdosimetric distributions. Four  $\bar{y}_D$  values calculated from  
 182 corrected microdosimetric spectra are displayed in figure 8 with open triangles following the trend of  
 183  $\bar{y}_D$  values obtained from not-corrected spectra. Furthermore, the typical "proton edge" can be seen  
 184 from an enlarged view of the microdosimetric spectra measured at the BP and its distal part (see inset  
 185 of figure 7).

186 The maximum lineal energy observed at this edge was approximately  $35 \text{ keV}/\mu\text{m}$  in water. This  
 187 lineal energy corresponds to a proton energy of 1.3 MeV with a stopping range of approximately  $12$   
 188  $\mu\text{m}$  in diamond equal to the sensor thickness. Therefore, this observed proton edge validates the  
 189 energy calibration performed with the  $\alpha$ -particle source and the pulse generator. Observed threshold  
 190 in experimentally derived microdosimetric spectra amounts to  $0.6 \text{ keV}/\mu\text{m}$  water equivalent. This is  
 191 comparable to frequently reported sensitivities of silicon based solid-state microdosimeters [29].

## 192 4. Discussion

### 193 4.1. Comparison of calculated $\bar{y}_D$ and literature results

194 The calculated dose-mean lineal energies  $\bar{y}_D$  from experimentally measured microdosimetric  
 195 spectra is presented in figure 8. The microdosimetric spectra and  $\bar{y}_D$  values measured with the diamond  
 196 GR microdosimeter are in agreement with expected trends. The measured microdosimetric spectra  
 197 shift to higher values of lineal energy with increasing penetration depth. The spectra shift and thus, a  
 198 steep increase of  $\bar{y}_D$  is expected towards the end of the proton range, where the protons deposit more

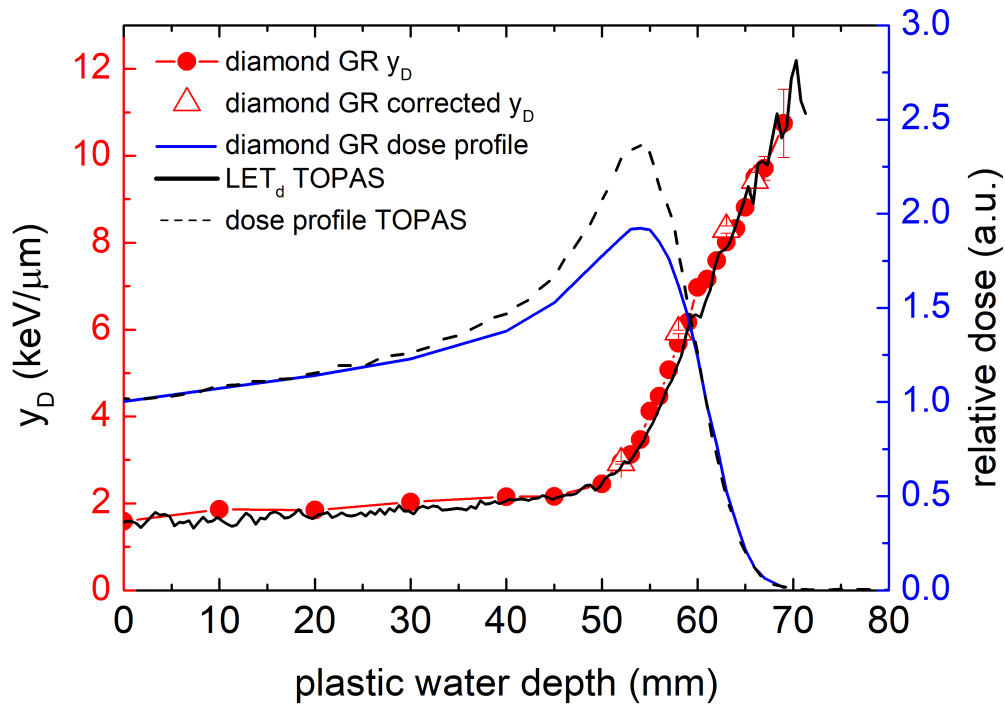


**Figure 8.**  $\bar{y}_D$  along dose profile both measured with diamond GR microdosimeter compared with dose profile and LET<sub>d</sub> from TOPAS simulations

199 energy in  $\mu\text{SVs}$ . The obtained result is also consistent with microdosimetric spectral trends observed  
 200 for silicon solid-state microdosimeters in clinical proton beams [30–32]. The dose-mean lineal energy  
 201  $\bar{y}_D$  values in the entrance region of the BP (0 mm to 40 mm) were approximately 2 keV/ $\mu\text{m}$ . Identical  
 202 values were reported for SOI microdosimeter for 159 MeV proton pencil beam [30]. In the proximal  
 203 and distal part of the BP (52 mm to 69 mm), the measured values went from 3 to 10.7 keV/ $\mu\text{m}$ , while  
 204 maximum measured  $\bar{y}_D$  value was reached at very distal part of BP at 69 mm depth at the point of only  
 205 1% relative dose distribution. Similar values were reported for SOI microdosimeter ranging from 3 to  
 206 10.3 keV/ $\mu\text{m}$ , with the maximum  $\bar{y}_D$  value reached at 20% of relative dose distribution in BP distal  
 207 fall-off. It must be noted, that if we compare the dose profile at the BP distal fall-off and  $\bar{y}_D$  values, in  
 208 general, diamond measured  $\bar{y}_D$  values for a degraded 230 MeV proton beam are lower compared to  
 209 reported  $\bar{y}_D$  values for SOI microdosimeter measured for lower proton beam energies. For instance, if  
 210 we consider the measured value of  $\bar{y}_D = 5.3$  keV/ $\mu\text{m}$  in diamond, it corresponds to a position at 50%  
 211 of relative dose in BP distal fall-off part of degraded 230 MeV proton beam. For SOI microdosimeter,  
 212 the  $\bar{y}_D$  at 50% of relative dose in BP distal fall-off part is 8.4 keV. Again such a trend is expected since,  
 213 with the increase of the initial beam energy, the maximum  $\bar{y}_D$ , decreases. The longer travelling path  
 214 from a higher-energy beam can result in more energy straggling close to the maximum range at the  
 215 corresponding locations. This will result in a higher mean energy and a lower  $\bar{y}_D$ , accordingly [33].

216 To further benchmark our experimental results of  $\bar{y}_D$ , we performed numerical simulations using  
 217 TOPAS Simulation Toolkit [34] to obtain dose-weighted LET<sub>d</sub> values. The complete Y1 beam line  
 218 geometry ( figure 3) with configuration identical to experiment was implemented in the simulation.  
 219 We used a water phantom placed in the isocenter to obtain dose and LET<sub>d</sub> profiles. The TOPAS  
 220 ProtonLET scorer gives the LET<sub>d</sub> of primary and secondary protons, including the energy deposited  
 221 by associated secondary electrons. More details about LET<sub>d</sub> scoring technique in TOPAS/Geant4  
 222 can be found in [35,36]. TOPAS simulated LET<sub>d</sub> profile is displayed in figure 8 (in black solid line)  
 223 is in close agreement with the experimentally measured  $\bar{y}_D$  profile for all depth. Frequently, due

224 to the fundamental difference between  $LET_d$  and  $\bar{y}_D$ , literature reported comparisons between both  
225 differ especially in the entrance part of the BP [31]. In general, this difference arises from the different  
226 volumes (voxels) used for  $LET_d$  calculation (typically  $\approx 1$  mm) and  $\bar{y}_D$  measurement (typically  $\approx$   
227 dozens of microns) and are related to the energy transfer differences by the delta-rays. Both quantities  
228 frequently differ at entrance part of the BP where delta-rays have higher range, exceeding the volume of  
229 interest used in measurement. In the distal part, delta-rays range becomes comparable with the volume  
230 of interest used in measurement, thus both values are in close agreement. In our case, volumes in  
231 simulation (0.05 mm) and measurement ( $\approx 39$  microns water-equivalent) were comparable, resulting in  
232 close agreement of  $\bar{y}_D$  and  $LET_d$  in the whole range. A comprehensive review of volume size influence  
233 on  $LET_d$  calculations can be found in [33].

234 The TOPAS simulated dose profile (shown in dash line of figure 8) reproduces very well the  
235 distal part of the measured diamond GR microdosimeter dose profile (shown in solid blue line) and  
236 the position of the BP. However, its amplitude differs from measured one. Both profiles have been  
237 normalized to the entrance point. At this stage of sensors development, we believe that the observed  
238 difference arises from characteristics of the diamond sensor, most probably due to the charge collection  
239 inefficiency or induced proton beam DC current saturation in the peak region for the measurement.  
240 Our second hypothesis (less probable) assumes that this difference arises from the over-response  
241 of the sensor in the entrance part due to the presence of non-tissue equivalent materials around  
242 diamond sensor. Further experiments with reference ionization chambers are planned to clarify this  
243 issue. Nevertheless, measured dose profile already allows precise sensor positioning and proton range  
244 verification.

## 245 5. Conclusions and current perspectives

246 A diamond GR microdosimeter with energy calibrated response has been fabricated and tested in  
247 a proton therapy facility. A demonstration of simultaneous measurement of the dose depth profile and  
248 microdosimetry spectra has been reported. The possibility of measuring both the depth dose profile  
249 and pulse-height spectra using one sensor allows precise positioning of the device for microdosimetric  
250 spectra acquisition in the selected points-of-interest - a very useful feature for future beam quality  
251 assurance system in hadron therapy. The measured calibrated pulse-height spectra of energy loss of  
252 protons in diamond have been benchmarked with Geant4 simulation, showing very good agreement,  
253 in terms of peak maximum position and widths. The dose-mean lineal energy  $\bar{y}_D$  have been compared  
254 and discussed with the experimental data measured with silicon based solid-state microdosimeters as  
255 reported in literature, as well as with numerical calculations of  $LET_d$  values. We observed all these  
256 values in close agreement at the entrance, the proximal and distal part of the BP. Finally, we reported a  
257 very good correlation between TOPAS simulated dose profile and our measurement for the distal part  
258 of the BP. A difference in dose profile amplitude at the BP could be associated with charge collection  
259 characteristics of the diamond sensor.

260 In ongoing work, the system is being miniaturized by integrating the CSA on the same printed  
261 circuit board with the sensor and the modular elements can be integrated in one water-proof PMMA  
262 housing to assure full portability. Thus, the entire system is expected to be compact, battery powered  
263 and with wireless data transfer capability. In order to improve the quality of the pulse height spectra,  
264 a new type of diamond membrane microdosimeter with truly isolated 3D microSVs, surrounded  
265 by a tissue equivalent non-electrically active material is envisaged in future developments of the  
266 microdosimetry system.

## 267 6. Patents

268 Patent pending: System for Dosimetric and Microdosimetric Ionizing Radiation Characterization–  
269 I.A. Zahrdnik, M. Pomorski, EP20305733.6, 30 June 2020

270 **Author Contributions:** Conceptualization, M.P and I.Z; methodology, X.X.; software, O.L, I.Z.; investigation, O.L,  
271 I. Z, M.P, M.L, AM.L; data curation, O.L.;I.Z, AM. L writing–original draft preparation, M.P, O.L; writing–review  
272 and editing, O.L, I.Z, AM.L, M.L, M.P; supervision, D.T.; project administration, M.P.; funding acquisition, M.P.

273 **Funding:** This research has been performed within the framework of DIAMiDOS (Diamond membrane  
274 microdosimeter) project funded by the French Alternative Energies and Atomic Energy Commission (CEA)  
275 and DIADEM (Diamond membrane based microdosimetric system for radiation quality assurance in hadron)  
276 project funded by INSERM.

277 **Conflicts of Interest:** The authors declare no conflict of interest.

## 278 References

- 279 1. Grau, C.; Durante, M.; Georg, D.; Langendijk, J.A; Weber, D.C; Particle therapy in Europe. *Molecular Oncology*  
280 **2020**, *10*, 142–149.
- 281 2. Marks, L.B; Ten, Haken R.; Martel, M.; et al. Quantitative analyses of normal tissue effects in the clinic. *Int J*  
282 *Radiat Oncol Biol Phys*, **2010**, *10*, 3, 1–160,
- 283 3. Freund, D.; Zhang, R; Sanders, M.; Newhauser, W. Predictive risk of radiation induced cerebral necrosis in  
284 pediatric brain cancer patients after VMAT versus proton therapy. *Cancers*, **2015**, *vol.7, no.2*, 617–630.
- 285 4. Schuemann, J.; Giantsoudi, D.; Niemierko, A.; Maquilan, G.; Shih, H.; Busse, P.; Niyazi, M.; Paganetti  
286 H. Brain Necrosis in Adult Proton Therapy Patients. Do Necrotic Regions Have Elevated Linear Energy  
287 Transfer?. *International Journal of Radiation Oncology, Biology, Physics*, **2019**, *105*,1, S230.
- 288 5. MacDonald, S.M.; Laack, N.N; Terezakis, S.; Humbling advances in technology: protons, brainstem necrosis,  
289 and the self-driving car. *International Journal of Radiation Oncology, Biology, Physics*, **2017**, *97*, 2, 216–219
- 290 6. Zaider, M.; Rossi, B.H.H; and Zaider, M.; *Microdosimetry and its Applications*, 1st ed.; Springer-Verlag:  
291 Berlin, Germany, **1996**, pp.11.
- 292 7. Paganetti, H.; Relating proton treatments to photon treatments via the relative biological  
293 effectiveness—should we revise current clinical practice?. *International Journal of Radiation Oncology• Biology•*  
294 *Physics*, **2015**, *91*,5,892–894.
- 295 8. Rørvik, E.; Fjæra, L. F.; Dahle, T.J; Dale, J.E; Engeseth, G. M.; Stokkevåg, C. H.; Thörnqvist, S.; Ytre-Hauge,  
296 S. Exploration and application of phenomenological RBE models for proton therapy. *Physics in Medicine &*  
297 *Biology*, **2018**, *63*, 18,185013.
- 298 9. S. Guatelli, S.; Reinhard, M. I.; Mascialino, B.; Prokopovich D. A.; Dzurak, A. S.; Zaider, M.; and Rosenfeld,  
299 A.B. Tissue Equivalence Correction in Silicon Microdosimetry for Protons Characteristic of the LEO Space  
300 Environment, *IEEE Transactions on Nuclear Science*, 2008, *55*, 6, 3407-3413,
- 301 10. Guardiola, C.; Quirion, D.; Pellegrini, G.; Fleta, C.; Esteban, S.; Cortés-Giraldo, M.A.; Gómez, F; Solberg,  
302 T.; Carabe, A.; Lozano, M. Silicon-based three-dimensional microstructures for radiation dosimetry in  
303 hadrontherapy, *Applied Physics Letters*, **2015**, *107*, 2, 023505.
- 304 11. Rosenfeld, A.B.; Bradley, P.D.; Cornelius, I.; Kaplan, G.I.; Allen, B.J.; Flanz, J.B.; Goitein, M.; Van Meerbeeck,  
305 A.; Schubert, J.; Bailey, J.; et al. A new silicon detector for microdosimetry applications in proton therapy,  
306 *IEEE Transactions on nuclear science*, **2000**, *47*, 4, 1386–1394.
- 307 12. Cornelius, I.; Siegele, R.; Rosenfeld, A. B; Cohen, D.D. Ion beam induced charge characterisation of a silicon  
308 microdosimeter using a heavy ion microprobe. *Nuclear Instruments and Methods in Physics Research*, **2002**, *190*,  
309 1-4, 335–338.
- 310 13. Fleta, C.; Guardiola, C.; Esteban, S.; Pellegrini, G.; Quirion, D.; Rodriguez, J.; Gomez, F; Carabe-Fernández,  
311 A.; Lozano, M. First investigations of Ultra-Thin 3D silicon detectors as microdosimeters. *Radiotherapy and*  
312 *Oncology*, **2014**, *110*, S36.
- 313 14. James, B.; Tran, L.T.; Bolst, D.; Peracchi, S.; Davis, J.A.; Prokopovich, D.A.; Guatelli, S.; Petasecca, M.; Lerch,  
314 M.; Povoli, M.; et al. SOI Thin Microdosimeters for High LET Single-Event Upset Studies in Fe, O, Xe, and  
315 Cocktail Ion Beam Fields. *IEEE Transactions on Nuclear Science*, **2019**, *67*, 1, 146–153.
- 316 15. Conte, V.; Bianchi, A.; Selva, A.; Petringa, G.; Cirrone, GAP.; Parisi, A.; Vanhavere, F.; Colautti, P.  
317 Microdosimetry at the CATANA 62 MeV proton beam with a sealed miniaturized TEPC. *Physica Medica*,  
318 **2019**, *64*, 114–122.
- 319 16. Bianchi, A.; Selva, A.; Colautti, P.; Bortot, D. Mazzucconi, D.; Pola, A.; Agosteo, S.; Petringa, G.; Cirrone, G.  
320 P; Reniers, B.; et al. Microdosimetry with a sealed mini-TEPC and a silicon telescope at a clinical proton  
321 SOBPs of CATANA. *Radiation Physics and Chemistry*, 2020, *171*, 108730.

- 322 17. Rollet, S.; Angelone, M.; Magrin, G.; Marinelli, M.; Milani, E.; Pillon, M.; Prestopino, G.; Verona, C.;  
323 Verona-Rinati, G. A novel microdosimeter based upon artificial single crystal diamond. *IEEE Transactions on*  
324 *Nuclear Science*, 2012, 59, 5, 2409–2415.
- 325 18. Magrin, G.; Microdosimetry in ion-beam therapy: studying and comparing outcomes from different  
326 detectors. *arXiv preprint arXiv:1802.06705*, 2018
- 327 19. Davis, J.A.; Ganesan, K.; Alves, A.; Prokopovich, D.A.; Guatelli, S.; Petasecca, M.; Lerch, M.L.; Jamieson,  
328 D.N.; Rosenfeld, A.B. Characterisation of an alternative novel diamond based microdosimeter prototype.  
329 *IEEE Transactions on Nuclear Science*, 2014, 61, 6, 3479–3484.
- 330 20. Verona, C.; Magrin, G.; Solevi, P.; Bandorf, M.; Marinelli, M.; Stock, M.; Rinati, G.V. Toward the use of single  
331 crystal diamond based detector for ion-beam therapy microdosimetry, *Radiation Measurements*, 2018, 110,  
332 25–31.
- 333 21. Manfredotti, C.; Giudice, A.L.; Ricciardi, C.; Paolini, C.; Massa, E.; Fizzotti, F.; Vittone, E. CVD diamond  
334 microdosimeters, *Nuclear Instruments and Methods in Physics Research*, 2001, 458, 1-2, 360–364.
- 335 22. Zahradnik, I.A.; Pomorski, M.T.; De Marzi, L.; Tromson, D.; Barberet, P.; Skukan, N.; Bergonzo, P.; Devès, G.;  
336 Herault, J.; Kada, W.; et al. scCVD diamond membrane based microdosimeter for hadron therapy. *Physica*  
337 *Status solidi (a)*, 2018, 215, 22, 1800383.
- 338 23. Davis, J.A.; Ganesan, K.; Prokopovich, D.A.; Petasecca, M.; Lerch, M. L. ; Jamieson, D.N.; Rosenfeld, A.B. A  
339 3D lateral electrode structure for diamond based microdosimetry. *Applied Physics Letters*, 2017, 110, 1, 013503.
- 340 24. Zahradnik, I.A.; Barberet, P.; Tromson, D.; De Marzi, L.; Pomorski, M.T. A diamond guard ring microdosimeter  
341 for ion beam therapy. *Review of Scientific Instruments*, 2020, 91, 5, 054102.
- 342 25. Davis, J. A. Diamond microdosimetry for radioprotection applications in space, Doctoral thesis, University  
343 of Wollongong, Australia, 2015.
- 344 26. <https://www.labzy.com/products/nanomcaii/>, consulted on 9th October, 2020.
- 345 27. <https://www.iba-dosimetry.com/>, consulted October, 2020
- 346 28. Collaboration, GEANT; Agostinelli, S.; et al., GEANT4—a simulation toolkit, *Nucl. Instrum. Meth. A*, 2003,  
347 506, 25, 0,
- 348 29. Bolst, D.; Guatelli, S.; Tran, L. T.; Chartier, L.; Davis, J.; Biasi, G.; Prokopovich, D.A.; Pogosso, A.; Reinhard,  
349 M. I.; Petasecca, M. and others, Validation of Geant4 for silicon microdosimetry in heavy ion therapy. *Physics*  
350 *in Medicine & Biology*, 2020, 65, 4, 045014.
- 351 30. Tran L.T.; Chartier, L.; Bolst, D.; Pogosso, A.; Guatelli, S.; Petasecca, M.; Lerch M.L.; Prokopovich, D.A.;  
352 Reinhard, M.I.; Clasie, B.; et al. Characterization of proton pencil beam scanning and passive beam using a  
353 high spatial resolution solid-state microdosimeter. *Medical physics*, 2017, 44, 11, 6085–6095.
- 354 31. Anderson, S.E.; Furutani, K.M.; Tran, L.T.; Chartier, L.; Petasecca, M.; Lerch, M.; Prokopovich, D. A; Reinhard,  
355 M.; Perevertaylo, V. L.; Rosenfeld, A. B.; and others. Microdosimetric measurements of a clinical proton  
356 beam with micrometer-sized solid-state detector. *Medical physics*, 2017, 44, 11, 6029–6037.
- 357 32. Debrot, E.; Tran, L.; Chartier, L.; Bolst, D.; Guatelli, S.; Vandevorode, C.; de Kock, E.; Beukes, P.; Symons, J.;  
358 Nieto-Camero, J.; and others. SOI microdosimetry and modified MKM for evaluation of relative biological  
359 effectiveness for a passive proton therapy radiation field. *Physics in Medicine & Biology*, 2018, 63, 23, 235007.
- 360 33. Guan, F.; Peeler, C.; Bronk, L.; Geng, C.; Taleei, R.; Randeniya, S.; Ge, S.; Mirkovic, D.; Grosshans, D.; Mohan,  
361 R.; and others. Analysis of the track-and dose-averaged LET and LET spectra in proton therapy using the  
362 geant4 Monte Carlo code. *Medical physics*, 2015, 42, 11, 6234–6247.
- 363 34. Perl, J.; Shin, J.; Schumann, J.; Faddegon, B.; Paganetti, H. TOPAS: an innovative proton Monte Carlo  
364 platform for research and clinical applications. *Medical physics*, 2012, 39, 11, 6818–6837.
- 365 35. Cortés-Giraldo, M.A.; Carabe, A. A critical study of different Monte Carlo scoring methods of dose average  
366 linear-energy-transfer maps calculated in voxelized geometries irradiated with clinical proton beams. *Physics*  
367 *in Medicine & Biology*, 2015, 60, 7, 2645.
- 368 36. Granville, D.A.; Sawakuchi, G. O. Comparison of linear energy transfer scoring techniques in Monte Carlo  
369 simulations of proton beams. *Physics in Medicine & Biology*, 2015 60, 14, N283.